China Ocean Eng., 2017, Vol. 31, No. 5, P. 528–538
DOI: 10.1007/s13344-017-0061-y, ISSN 0890-5487
http://www.chinaoceanengin.cn/ E-mail: coe@nhri.cn

Stability Analysis of Hybrid-Driven Underwater Glider

NIU Wen-dong[a], WANG Shu-xin[a], WANG Yan-hui[a, b, *], SONG Yang[a], ZHU Ya-qiang[a]

[a]Key Laboratory of Mechanism Theory and Equipment Design of Ministry of Education, School of Mechanical Engineering, Tianjin University, Tianjin 300072, China

[b]The Joint Laboratory of Ocean Observing and Detecting, Qingdao National Laboratory for Marine Science and Technology, Qingdao 266237, China

Received March 17, 2016; revised March 6, 2017; accepted May 26, 2017

Abstract

Hybrid-driven underwater glider is a new type of unmanned underwater vehicle, which combines the advantages of autonomous underwater vehicles and traditional underwater gliders. The autonomous underwater vehicles have good maneuverability and can travel with a high speed, while the traditional underwater gliders are highlighted by low power consumption, long voyage, long endurance and good stealth characteristics. The hybrid-driven underwater gliders can realize variable motion profiles by their own buoyancy-driven and propeller propulsion systems. Stability of the mechanical system determines the performance of the system. In this paper, the Petrel-II hybrid-driven underwater glider developed by Tianjin University is selected as the research object and the stability of hybrid-driven underwater glider unitedly controlled by buoyancy and propeller has been targeted and evidenced. The dimensionless equations of the hybrid-driven underwater glider are obtained when the propeller is working. Then, the steady speed and steady glide path angle under steady-state motion have also been achieved. The steady-state operating conditions can be calculated when the hybrid-driven underwater glider reaches the desired steady-state motion. And the steady-state operating conditions are relatively conservative at the lower bound of the velocity range compared with the range of the velocity derived from the method of the composite Lyapunov function. By calculating the hydrodynamic coefficients of the Petrel-II hybrid-driven underwater glider, the simulation analysis has been conducted. In addition, the results of the field trials conducted in the South China Sea and the Danjiangkou Reservoir of China have been presented to illustrate the validity of the analysis and simulation, and to show the feasibility of the method of the composite Lyapunov function which verifies the stability of the Petrel-II hybrid-driven underwater glider.

Key words: hybrid-driven underwater glider, stability analysis, numerical simulation, field trials

Citation: Niu, W. D., Wang, S. X., Wang, Y. H., Song, Y., Zhu, Y. Q., 2017. Stability analysis of hybrid-driven underwater glider. China Ocean Eng., 31(5): 528–538, doi: 10.1007/s13344-017-0061-y

1 Introduction

The Autonomous Underwater Gliders (AUGs) equipped with advanced sensors play an important role in the development of marine survey and marine disaster forecasting. The Hybrid-driven Underwater Gliders (HUGs) are regarded as a specialized kind of AUGs, which have been reliable and affordable. At present, the traditional AUGs have been widely used in scientific research and military fields (Liu, 2014), while the practical application of the HUGs is relatively limited. The Folaga-III as a HUG is specifically oriented toward the investigation of ocean mesoscale dynamics in shallow coastal waters (Caffaz et al., 2010).

There are three kinds of traditional AUGs, including *Slocum* (Webb et al., 2001), *Spray* (Sherman et al., 2001) and *Seaglider* (Eriksen et al., 2001). They can achieve zigzag diving and floating movements by changing their net buoyancy and relying on the lateral force component generated by the fixed wings. With low speed, poor mobility and single movement, the traditional AUGs could not effectively fulfill the tasks in the conduction of certain specific oceanographic surveys. But for HUGs, by combining the advantages of autonomous underwater vehicles (AUVs) and traditional AUGs and manipulated by their own buoyancy-driven and propeller propulsion systems, they can complete a variety of complex tasks with different motion modes, such as target tracking, and sailing in a fixed depth.

Two typical HUGs are Slocum AUV of Webb Research Corporation (Jenkins et al., 2003; Liu, 2014) and Folaga-III

Foundation item: This work was financially supported by the National Natural Science Foundation of China (Grant Nos. 51475319 and 51722508), the National Key R&D Plan (Grant No. 2016YFC0301100), and Aoshan Talents Program of Qingdao National Laboratory for Marine Science and Technology.

*Corresponding author. E-mail: yanhuiwang@tju.edu.cn of NURC (Alvarez et al., 2009). Tianjin University has successfully developed its first generation of HUG named Petrel in 2007, and then developed Petrel-II as an improvement in 2013, as shown in Fig. 1. So far, the Petrel-II HUG has completed a series of sea trials (Niu et al., 2016). The results of the comparison between the Petrel-II and other HUGs in specific performance are described in Table 1.

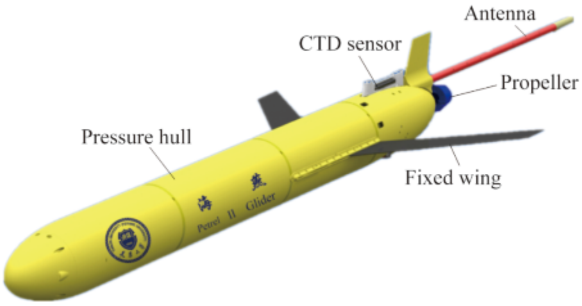

Fig. 1. The whole shape of Petrel-II HUG.

Table 1 Results of comparison between the Petrel-II and other HUGs in specific performance

Property	HUGs		
	Slocum AUV	Folaga-III	Petrel-II
Diameter (mm)	220	140	221
Mass (kg)	56	30	70
Design depth (m)	1000	100	1500
Advance rate (m/s)	1.00	1.01	1.50
Length (not including antenna) (m)	1.5	2.0	2.3
Battery power (MJ)	36.70	3.11	18.9
Voyage (km)	1500–6000	--	1500

The HUGs is faster than the traditional gliders. But when the velocity exceeds a certain threshold, the HUGs may be easily unstable. In addition, the stability is a major concern in the preliminary design phase. And it is important to obtain the region of attraction of the HUG, which is influenced by many factors, such as the dimension of the HUG, and the propeller speed.

Several studies on the stability of the underwater vehicles are reviewed in this part. For example, Leonard and Marsden (1997) developed the stability theory of relative equilibriums for mechanical systems with symmetry and applied it to underwater vehicle dynamics. The stabilization of underwater vehicle dynamics with symmetry-breaking potentials and the stability of a bottom-heavy underwater vehicle were studied by Leonard(1997a, 1997b). Woolsey and Leonard (2002) stabilized the underwater vehicle motion by using the internal rotors. For the stability analysis of the mechanical system, a typical method is the Lyapunov method. By linearizing the kinetic equations of underwater glider, the eigenvalues of the system matrix are calculated (Fan et al., 2012; Leonard and Graver, 2001) and then by judging the eigenvalues of the coefficient matrix, the stability of the system is determined. For example, if all the eigenvalues have negative real parts, then it can be concluded that the traditional underwater glider is asymptotically stable in its balanced states. Bhatta and Leonard proved the stability of underwater glider by Lanchester's phugoid-mode dynamics and singular perturbation theory (Bhatta and Leonard, 2004, 2008; Bhatta, 2006). Furthermore, they designed a stable controller for the traditional underwater gliders subjected to different external forces and torques. As a result, the underwater glider can achieve a steady gliding in the vertical plane. Caiti and Calabro (2010) proposed the control law of a hybrid AUV and proved the Lyapunov stability of the control. Zhao et al. (2015) obtained the law in which the stability varies with design parameters and the control parameters by establishing the relationship between the stability of actual underwater glider and parameters of design and control. Among them, the stability is judged by Lyapunov first and second theorems.

However, the stability of HUG simultaneously controlled by buoyancy-driven and propeller propulsion systems (namely in the hybrid-driven mode) has been seldom reported in the literature. Isa regarded and expressed the propeller thrust as the constant force to control the buoyancy-driven system (Isa and Arshad, 2012, 2013; Isa et al., 2014). But in fact, the propeller thrust is a function of the propeller speed. In this paper, Petrel-II HUG is selected as the research object, and the stability of HUG is proved based on the fact that Bhatta and Leonard have proved the stability of the underwater glider by Lanchester's phugoid-mode dynamics and singular perturbation theory when the glider is controlled only by the buoyancy-driven system (namely in the gliding mode) (Bhatta and Leonard, 2004, 2008; Bhatta, 2006). However, there are some differences between the HUGs in the hybrid-driven mode and the traditional gliders in the gliding mode. Compared with working in the gliding mode, when working in the hybrid-driven mode, the HUG has a larger maximum steady speed, a smaller corresponding steady angle of attack, and larger ranges of steady glide path angle and pitch angle. When the horizontal velocity reaches the maximum, the corresponding steady glide path angle of the HUG is smaller in the hybrid-driven mode than that in the gliding mode.

The remainder of this paper is structured as follows. In Section 2 the kinetic model of HUG and dimensionless equations of equilibrium motion are described. Section 3 proves the stability of HUG working in the hybrid-driven mode based on the method of composite Lyapunov function, and calculates the steady-state operating conditions as the HUG reaches the desired steady-state motion. In Section 4, according to the model of the Petrel-II, the steady speed and steady angle of attack of HUG in the gliding mode and those in the hybrid-driven mode are comparatively analyzed, while the region of attraction provided by the Lyapunov function is estimated. In Section 5 we present the experimental results and figures recorded in the field trials to show the feasibility of the method. The conclusions are summarized in Section 6.

2 Hybrid-driven underwater glider model and dimensionless equations

The HUG can achieve diving and ascending movements by changing its own net buoyancy or controlling the propeller speed, or controlling both of them simultaneously. Through shifting and rotating the internal battery pack, the attitude control of the HUG can be realized. The masses of HUG mainly include the hull mass m_{h}, the mass of the movable battery pack $\bar{m}$, the variable mass of the buoyancy-driven system m_{b} and the mass fixed in one position m_{w}. And the total vehicle mass is $m = m_{\mathrm{h}}+\bar{m}+m_{\mathrm{b}}+m_{\mathrm{w}}$. Those masses are illustrated in Fig. 2.

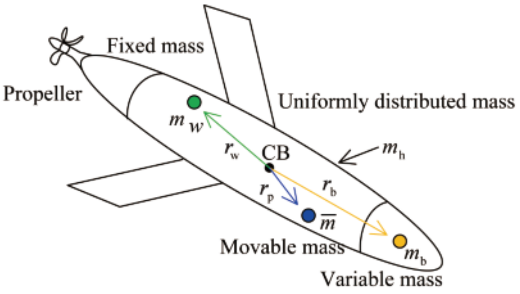

Fig. 2. Mass distribution of the HUG.

A coordinate frame is fixed on the vehicle body as the body frame and its origin is located at the center of buoyancy (CB). The body axis e_1 is aligned with the long axis of the vehicle, the positive direction is toward the nose of the HUG, e_2 lies in the plane of wings and e_3 points to the direction orthogonal to the wings conformed to the right-hand rule. The body frame is shown in Fig. 3.

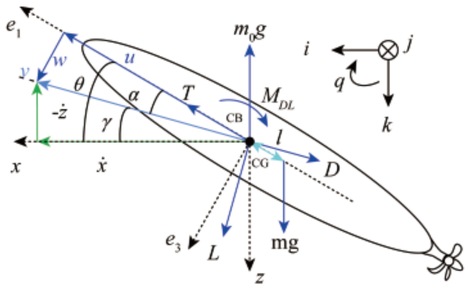

Fig. 3. Force analysis of the HUG in the longitudinal plane, vectors i, j, and k represent the inertial coordinate system.

The position of the HUG $\boldsymbol{b}=(x, y, z)^{\mathrm{T}}$ is the vector from the origin of the inertial frame to the origin of the body frame. The vectors $\boldsymbol{V}=(u, v, w)^{\mathrm{T}}$ and $\boldsymbol{\Omega}=(p, q, r)^{\mathrm{T}}$ represent the translational velocity and angular velocity of the body frame, as shown in Fig. 3. The vector from the CB to the mass of the movable battery pack is $\boldsymbol{r}_{\mathrm{p}}=(r_{\mathrm{p}1}, r_{\mathrm{p}2}, r_{\mathrm{p}3})^{\mathrm{T}}$. The vector from the CB to the variable mass of the buoyancy-driven system is $\boldsymbol{r}_{\mathrm{b}}=(r_{\mathrm{b}1}, r_{\mathrm{b}2}, r_{\mathrm{b}3})^{\mathrm{T}}$ and the vector from the CB to the fixed mass is $\boldsymbol{r}_{\mathrm{w}}=(r_{\mathrm{w}1}, r_{\mathrm{w}2}, r_{\mathrm{w}3})^{\mathrm{T}}$, as shown in Fig. 2.

We make the following assumptions:

(1) The HUG is symmetric about the longitudinal axis and the mass distribution of the HUG is uniform (Bhatta and Leonard, 2008).

(2) While the propeller is working, the propeller torque has no effect on the HUG; in other words, there is no yaw motion.

(3) Fix the variable mass of the buoyancy-driven system and the mass of the movable battery pack to the origin of the body frame, that is the vector $\boldsymbol{r}_{\mathrm{b}}=0$ and $\boldsymbol{r}_{\mathrm{p}}=0$ (Bhatta and Leonard, 2008).

(4) $m_{\mathrm{w}}=0$.

The HUG is considered as an ellipsoidal rigid body, with wings fixed on the fuselage and the propeller fixed on the rear. The rigid body is subjected to the buoyancy (m_0g), gravity (mg), lift (L), drag (D) and thrust (T). It also experiences a hydrodynamic pitching moment in the longitudinal plane (Bhatta and Leonard, 2008). Lift acts perpendicular to the velocity while the drag always acts in the direction opposite to the velocity. The propeller thrust acts in the direction of the axis e_1. They are all shown in Fig. 3.

Based on the above assumptions, we can derive the motion equations of the HUG in the longitudinal plane (Leonard and Graver, 2001):

$$\dot{V} = -\frac{1}{m_3}(m_0 g\sin\gamma - D + T\cos\alpha) - \frac{\Delta m\cos\alpha}{m_1 m_3}[m_0 g\sin\theta - L\sin\alpha + D\cos\alpha + (m_1+m_3)Vq\sin\alpha]; \tag{1}$$

$$\dot{\gamma} = \frac{1}{m_3 V}(m_0 g\cos\gamma - L + T\sin\alpha) - \frac{\Delta m}{m_1 m_3 V}\Big[(m_0 g\sin\theta - L\sin\alpha + D\cos\alpha)\sin\alpha + (m_3\sin^2\alpha - m_1\cos^2\alpha)Vq\Big]; \tag{2}$$

$$\dot{\alpha} = q - \dot{\gamma}; \tag{3}$$

$$\dot{q} = \frac{1}{J_2}(\Delta m V^2\sin\alpha\cos\alpha + M_{DL} + mgl\cos\theta), \tag{4}$$

where,

$$L = (K_{\mathrm{L0}} + K_{\mathrm{L}}\alpha)V^2; \tag{5}$$

$$D = (K_{\mathrm{D0}} + K_{\mathrm{D}}\alpha^2)V^2; \tag{6}$$

$$M_{DL} = (K_{\mathrm{M0}} + K_{\mathrm{M}}\alpha + K_q q)V^2; \tag{7}$$

$$T = K_{\mathrm{T}}\rho n^2 D_0^{\,4}. \tag{8}$$

In Eqs. (1)–(8), m_1 and m_3 are the components of mass along the e_1 and e_3 direction, respectively. Here the mass is the sum of the glider and added mass generated by the water (Leonard et al., 2001) and $\Delta m=m_1-m_3$; θ indicates the pitch angle (rad) (see Fig. 3); q is the rate of the pitch angle;

γ is the path angle of the glide (rad); g is the acceleration of gravity, g=10 m/s^2; α is the angle of attack (rad); l is the distance from CB to CG projected on the axis e_1 (mm); $K_{\rm L}$ is the lift coefficient [kg/(m/rad)] and $K_{\rm L0}$ for α=0; $K_{\rm D}$ is the drag coefficient [kg/(m/rad^2)] and $K_{\rm D0}$ for α=0; $K_{\rm M}$ is the viscous moment coefficient (kg/rad), and $K_{\rm M0}$ for α=0; K_q is the angular velocity moment coefficient (kg·s/rad); $K_{\rm T}$ is the propeller thrust coefficient; ρ is the density of sea water, ρ=1020 kg/m^3; n is the propeller speed (rpm); and D_0 is the diameter of propeller (mm).

Generally, $K_{\rm L0}$ is 0 or a very small positive number, $K_{\rm L}$, $K_{\rm D0}$, $K_{\rm D}$ are positive, $K_{\rm M}$ and K_q are negative, while $K_{\rm M0}$ can be positive or negative (Bhatta and Leonard, 2008).

Table 2 Relationship betweent $K_{\rm T}$ and J_0

J_0	0.40	0.60	1.20	1.40
$K_{\rm T}$	0.45	0.36	0.13	0.04

Firstly, we non-dimensionalize the motion equations and shift the equilibrium to the origin. We define the dimensionless speed ($\overline{V}$), the dimensionless path angle of glide ($\bar{\gamma}$), the dimensionless angle of attack ($\bar{\alpha}$), and the dimensionless angular velocity ($\overline{q}$) as follows: $\overline{V}=(V-V_{\rm e})/V_{\rm e}$, $\bar{\gamma}=\gamma-\gamma_{\rm e}$, $\bar{\alpha}=\alpha-\alpha_{\rm e}$, $\bar{q}=K_q q/K_{\rm M}$, $V_{\rm e}$, $\gamma_{\rm e}$ and $\alpha_{\rm e}$ being the steady speed, the steady path angle of glide, and the steady angle of attack, respectively; and then we introduce two small positive numbers: $\varepsilon_1=K_q/(K_{\rm M}\tau_{\rm s})$ and $\varepsilon_2=-J_2/(K_q V_{\rm e}^2\tau_{\rm s})$, where $\tau_{\rm s}=m_3/K_{\rm De}V_{\rm e}$, $K_{\rm De}$ being the drag coefficient of the steady glide (kg/m), and $K_{\rm De}=K_{\rm D0}+K_{\rm D}\alpha_{\rm e}^2$. The dimensionless time variable is defined as $t_{\rm n}=t/\tau_{\rm s}$.

Finally, assuming that the HUG has the same added mass and that the CB coincides with the CG (the center of gravity), we rewrite the Eqs. (1)–(4) in terms of the dimensionless state variables concerning the nonzero propeller thrust.

$$\frac{{\rm d}\overline{V}}{{\rm d}t_{\rm n}}=-\frac{1}{K_{\rm De}V_{\rm e}^2}\left[-m_0 g\sin(\bar{\gamma}+\gamma_{\rm e})+D'-T\cos(\bar{\alpha}+\alpha_{\rm e})\right]; \tag{9}$$

$$\frac{{\rm d}\bar{\gamma}}{{\rm d}t_{\rm n}}=\frac{1}{K_{\rm De}V_{\rm e}^2(1+\overline{V})}\left[m_0 g\cos(\bar{\gamma}+\gamma_{\rm e})-L'+T\sin(\bar{\alpha}+\alpha_{\rm e})\right]; \tag{10}$$

$$\varepsilon_1\frac{{\rm d}\bar{\alpha}}{{\rm d}t_{\rm n}}=\bar{q}-\varepsilon_1\frac{{\rm d}\bar{\gamma}}{{\rm d}t_{\rm n}}; \tag{11}$$

$$\varepsilon_2\frac{{\rm d}\bar{q}}{{\rm d}t_{\rm n}}=-(\bar{\alpha}+\bar{q})(1+\overline{V})^2, \tag{12}$$

where,

$$L'=\left[K_{\rm L0}+K_{\rm L}(\bar{\alpha}+\alpha_{\rm e})\right]V_{\rm e}^2(1+\overline{V})^2; \tag{13}$$

$$D'=\left[K_{\rm D0}+K_{\rm D}(\bar{\alpha}+\alpha_{\rm e})^2\right]V_{\rm e}^2(1+\overline{V})^2. \tag{14}$$

Eqs. (9)–(12) are the dimensionless equations of the hybrid-driven underwater glider in the hybrid-driven mode. And the specific propeller thrust T is shown below.

According to the above assumption (2), we consider that the propeller torque has no effect on the yaw motion of the HUG. Then according to the actual propeller propulsion system configured on the Petrel-II HUG, the pitch ratio P/D_0=1.4; the advance ratio of the propeller $J_0=V/(D_0 n)$, according to the atlas of $K_{\rm T}$–J (Wang, 2012), we can obtain the relationship between $K_{\rm T}$ and J_0 shown in Table 2.

Then the fitting curve between $K_{\rm T}$ and J_0 can be obtained:

$$K_{\rm T}=K_2 J_0+K_1, \tag{15}$$

where, K_1 is the propeller thrust coefficient constant, K_1=0.6136; and K_2 is the scale factor of propeller thrust coefficient, K_2=–0.4091.

Substituting Eq. (15) into Eq. (8), we can derive the relationship between the propeller thrust and the velocity:

$$T=\left[\frac{1}{J_0^2}(K_1\rho D_0^2)+\frac{1}{J_0}(K_2\rho D_0^2)\right]V^2. \tag{16}$$

Through Eq. (16), with the given speed V, the advance ratio J_0 is a constant value since the propeller speed n is a constant value. Then we can obtain the propeller thrust T. According to Eq. (8), we know that the thrust T is a function of propeller speed n, the speed V, the density of fluid ρ, and the diameter of propeller D_0. When the propeller diameter is fixed, the density of fluid will be assumed to be constant and the thrust $T\approx cn^2$ (Wang et al., 2015).

By simplifying Eqs. (9)–(12), the following equations can be obtained:

$$\frac{{\rm d}\boldsymbol{x}}{{\rm d}t_{\rm n}}=\boldsymbol{f}(\boldsymbol{x},\boldsymbol{y}); \tag{17}$$

$$\mu\frac{{\rm d}\boldsymbol{y}}{{\rm d}t_{\rm n}}=\boldsymbol{A}\boldsymbol{g}(\boldsymbol{x},\boldsymbol{y},\boldsymbol{\varepsilon}), \tag{18}$$

where, $\boldsymbol{x}=\begin{bmatrix}\overline{V}\\ \bar{\gamma}\end{bmatrix}$, $\boldsymbol{y}=\begin{bmatrix}\bar{\alpha}\\ \bar{q}\end{bmatrix}$, $\boldsymbol{A}=\begin{bmatrix}\mu/\varepsilon_1 & 0\\ 0 & \mu/\varepsilon_2\end{bmatrix}$, $\boldsymbol{f}=\begin{bmatrix}f_1\\ f_2\end{bmatrix}$, $\boldsymbol{g}=\begin{bmatrix}g_1\\ g_2\end{bmatrix}$, $\mu=\max\{\varepsilon_1,\varepsilon_2\}$. f_1 and f_2 are defined as follows:

$$f_1=-\frac{1}{K'_{\rm De}V_{\rm e}^2}\left[-m_0 g\sin(\bar{\gamma}+\gamma_{\rm e})+K'_{\rm De}V_{\rm e}^2(1+\overline{V})^2\right], \tag{19}$$

$$f_2=-\frac{1}{K'_{\rm De}V_{\rm e}^2(1+\overline{V})}\left[-m_0 g\cos(\bar{\gamma}+\gamma_{\rm e})+K'_{\rm Le}V_{\rm e}^2(1+\overline{V})^2\right], \tag{20}$$

where, $g_1=\bar{q}-\varepsilon_1 f_2$; $g_2=-(\bar{\alpha}+\bar{q})(1+\overline{V})^2$; $K'_{\rm De}$ is the drag coefficient of the steady advance glide (kg/m), and $K'_{\rm De}=K_{\rm D0}+K_{\rm D}\alpha_{\rm e}^2-u_{2\rm e}\cos\alpha_{\rm e}$; $K'_{\rm Le}$ is the lift coefficient of the steady advance glide (kg/m), and $K'_{\rm Le}=K_{\rm L0}+K_{\rm L}\alpha_{\rm e}-u_{2\rm e}\sin\alpha_{\rm e}$; $u_{2\rm e}=\dfrac{K_1\rho D_0^4}{V_{\rm e}^2}n_{\rm e}^2+\dfrac{K_2\rho D_0^3}{V_{\rm e}}n_{\rm e}$.

Moreover, we can divide the system of the HUG into two parts, among which the boundary-layer system is expressed by Eq. (18) and the reduced system is expressed by Eq. (17).

By Eqs. (9) and (10), the steady speed and steady glide path angle of the HUG can be obtained under steady-state motion:

$$V_{\mathrm{e}} = \sqrt{\frac{-B+\sqrt{B^2-4AC}}{2A}}; \tag{21}$$

$$\gamma_{\mathrm{e}} = -\arctan\frac{K'_{\mathrm{De}}}{K'_{\mathrm{Le}}}, \tag{22}$$

where, $A = (K_{\mathrm{D0}} + K_{\mathrm{D}}\alpha_{\mathrm{e}}^2)^2 + (K_{\mathrm{L0}} + K_{\mathrm{L}}\alpha_{\mathrm{e}})^2$,
$B - 2T\left[(K_{\mathrm{D0}} + K_{\mathrm{D}}\alpha_{\mathrm{e}}^2)\cos\alpha_{\mathrm{e}} + (K_{\mathrm{L0}} + K_{\mathrm{L}}\alpha_{\mathrm{e}})\sin\alpha_{\mathrm{e}}\right]$,
$C = T^2 - (m_0 g)^2$.

For a specific HUG, when the motion of the HUG is steady, q is 0 and K_{L0}, K_{L}, K_{D0}, K_{D}, K_{M0} and K_{M} come to be constants. According to Eq. (4), we can derive that the steady angle of attack $\alpha_{\mathrm{e}} = -K_{\mathrm{M0}}/K_{\mathrm{M}}$. Given the steady speed and steady glide path angle, the net mass under the steady-state motion $m_{0\mathrm{e}}$ and propeller speed n_{e} can be derived.

3 Stability analysis of HUG based on the method of composite Lyapunov function

The desired steady-state motion of the HUG is asymptotically stable when the HUG is working in the hybrid-driven mode, and the following inequalities are satisfied:

$$K'_{\mathrm{De}} = K_{\mathrm{D0}} + K_{\mathrm{D}}\alpha_{\mathrm{e}}^2 - u_{2\mathrm{e}}\cos\alpha_{\mathrm{e}} > 0; \tag{23}$$

$$B^2 - 4AC \geqslant 0; \tag{24}$$

$$-B + \sqrt{B^2 - 4AC} > 0. \tag{25}$$

By simplifying Inequalities (24) and (25), we can obtain the following inequalities eventually:

$$K_{\mathrm{D0}} + K_{\mathrm{D}}\alpha_{\mathrm{e}}^2 - u_{2\mathrm{e}}\cos\alpha_{\mathrm{e}} > 0; \tag{26}$$

$$V_{\mathrm{e}} > \sqrt{\frac{T_{\mathrm{e}}}{K_{D0}}}; \tag{27}$$

$$T_{\mathrm{e}} \leqslant \inf\left(\frac{G\sqrt{d^2+l^2}}{|d\sin\alpha_{\mathrm{e}} - l\cos\alpha_{\mathrm{e}}|}\right), \tag{28}$$

where T_{e} is the propeller thrust of the steady advance glide (N). inf ( ) represents the lower bound of the function; $d = (K_{\mathrm{D0}} + K_{\mathrm{D}}{\alpha_{\mathrm{e}}}^2)^2$; $l = (K_{\mathrm{L0}} + K_{\mathrm{L}}{\alpha_{\mathrm{e}}}^2)^2$; and $G = m_0 g$.

The inequalities are peculiar to the system when operating steadily. When Inequalities (26)–(28) being hold, the HUG can achieve a steady motion.

Brief proof is shown as follows:

When the HUG is in the hybrid-driven mode, the equilibrium Eqs. (11) and (12) of boundary-layer system are similar to the equilibrium equations of boundary-layer system in the literature (Bhatta and Leonard, 2008), while only g_1 shown in Eq. (29) is different. As a result, the boundary-layer system of the HUG is exponentially stable.

$$g_1 = \bar{q} + \varepsilon_1\frac{1}{K'_{\mathrm{De}}V_{\mathrm{e}}^2(1+\overline{V})}\left[-m_0 g\cos(\bar{\gamma}+\gamma_{\mathrm{e}}) + K'_{\mathrm{Le}}V_{\mathrm{e}}^2(1+\overline{V})^2\right]. \tag{29}$$

And the equilibrium equations of the reduced system are shown as follows:

$$\frac{\mathrm{d}\overline{V}}{\mathrm{d}t_{\mathrm{n}}} = -\frac{1}{K_{\mathrm{De}}V_{\mathrm{e}}^2}\left[-(\overline{m}_0 + m_{0\mathrm{e}})g\sin(\bar{\gamma}+\gamma_{\mathrm{e}}) + K'_{\mathrm{De}}V_{\mathrm{e}}^2(1+\overline{V})^2\right]; \tag{30}$$

$$\frac{\mathrm{d}\bar{\gamma}}{\mathrm{d}t_{\mathrm{n}}} = -\frac{1}{K_{\mathrm{De}}V_{\mathrm{e}}^2(1+\overline{V})}\left[-(\overline{m}_0 + m_{0\mathrm{e}})g\cos(\bar{\gamma}+\gamma_{\mathrm{e}}) + K'_{\mathrm{Le}}V_{\mathrm{e}}^2(1+\overline{V})^2\right], \tag{31}$$

where $\overline{m}_0$ is the dimensionless net mass (Bhatta and Leonard, 2008).

The above equations are identical to the equations of the reduced system mentioned in the literature (Bhatta and Leonard, 2008; Bhatta, 2006), except that we now have K'_{De} and K'_{Le} instead of K_{De} and K_{Le}, where $K_{\mathrm{Le}} = K_{\mathrm{L0}} + K_{\mathrm{L}}\alpha_{\mathrm{e}}$. In Section 2, $t_{\mathrm{n}} = t/\tau_{\mathrm{s}}$, and $\tau_{\mathrm{s}} = m_3/(K_{\mathrm{De}}V_{\mathrm{e}})$, but now the new $\tau_{\mathrm{s}} = m_3/(K'_{\mathrm{De}}V_{\mathrm{e}})$ and we must ensure $K'_{\mathrm{De}} > 0$. Thus under the premise of satisfying Inequalities (26)–(28), we can conclude that the reduced system is exponentially stable. Then the proof of the interconnection conditions derived from Theorem 1 of Khalil (1987) is shown in Appendix A.

As a result, the HUG working in the hybrid-driven mode can achieve asymptotical stability when ε_i is sufficiently small according to the method of composite Lyapunov function shown as follows (Khalil, 1987; Khalil and Grizzle, 1996):

$$v = (1-d)\left[\frac{2}{3} - (1+\overline{V})\cos\bar{\gamma} + \frac{1}{3}(1+\overline{V})^3\right] + \frac{d}{2}\left\{\left[r_1 + (1+\overline{V})^2(r_1+r_2)\right]\bar{\alpha}^2 + \left[1 + \frac{r_1}{r_2(1+\overline{V})^2}\right]\bar{q}^2 + 2\bar{\alpha}\bar{q}\right\}, \tag{32}$$

where, $r_1 = \mu/\varepsilon_1$, $r_2 = \mu/\varepsilon_2$, $0<d<1$, $a_1=1$, $a_2=r_2$;

$$\beta_1 = \frac{K'_{\mathrm{De}}(|\bar{\alpha}_{\max}| + 2|\alpha_{\mathrm{e}}|) + u_{2\mathrm{e}}H}{K'_{\mathrm{De}}}\left[\left(\sqrt{2}+1\right)\overline{V}_{\max} + \sqrt{2}\right] + \frac{K_{\mathrm{L}} + u_{2\mathrm{e}}H'}{K'_{\mathrm{De}}};$$

$$\beta_2 = \beta'_2 = \frac{c_1 + c_3}{K'_{\mathrm{De}}\left(1+\overline{V}_{\min}\right)^3}\left\{|K_{\mathrm{Le}}|\left[\left(\sqrt{2}+1\right)\overline{V}_{\max} + \sqrt{2}\right] + |u_{2\mathrm{e}}|\left[\left(\sqrt{2}+1\right)\left(\overline{V}_{\max}+1\right)+1\right] + |K_{\mathrm{De}}|\right\},$$

the details are shown in Appendix A.

4 Numerical example of Petrel-II HUG model

In this section, the following hydrodynamic coefficients of the Petrel-II are calculated based on the CFD simulation:

K_{L0}=0 kg/m, K_{L}=351.3570 kg/(m/rad), K_{D0}=7.3579 kg/m, and K_{D}=318.0849 kg/(m/rad^2).

Through the above hydrodynamic coefficients, Eqs. (21)–(22) and $\theta = \gamma + \alpha$, under the conditions of T=0 N and m_0=0.7 kg, we can obtain the relationship curve between the steady speed of the Petrel-II HUG and the steady angle of attack and the relationship curve between the steady glide angles including the steady glide path angle, pitch angle and the steady angle of attack. They are shown specifically in

Fig. 4 and Fig. 5, respectively. These curves are derived when only the buoyancy-driven system is working.

When the HUG reaches a steady state in the hybrid-driven mode, and the propeller thrust satisfies Inequality (28) and is expressed by equations like T_e=7 N, the propeller speed is n_e=1391 rpm. Then according to Eqs. (21)–(22) and $\theta = \gamma + \alpha$, we can obtain the relationship curve between the steady speed of the Petrel-II HUG and the steady angle of attack and the relationship curve between the steady glide angles including the steady glide path angle, pitch angle and steady angle of attack. They are shown specifically in Fig. 6 and Fig. 7, respectively.

In Fig. 6, the dotted line represents Inequality (27). The speed of the HUG can reach a steady state only when the curves are on the top of the dotted line. The shapes of the curves on the top of the dotted line are similar to the shapes of the curves shown in Fig. 4 in the gliding mode. The maximum velocity is obtained when the steady angle of attack is 0°. In Fig. 7, when the steady angle of attack is smaller than 0°, the steady glide path angle and pitch angle are larger than 0°. However, it is impossible for them to be smaller than 0°. When the steady angle of attack is larger than 0°, the steady glide path angle and pitch angle are smaller than 0°. It is also unlikely for them to exceed 0°. And both shapes in Fig. 7 and Fig. 5 are similar as well.

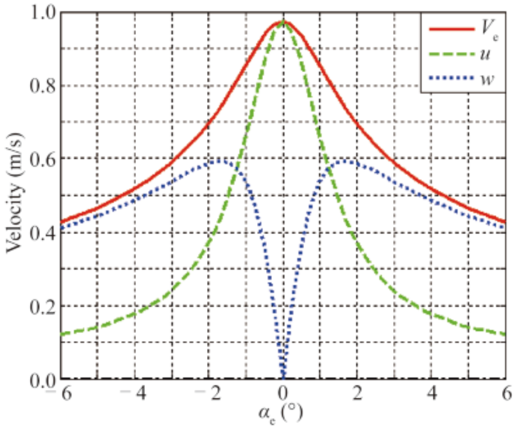

Fig. 4. Steady speed vs. the steady angle of attack.

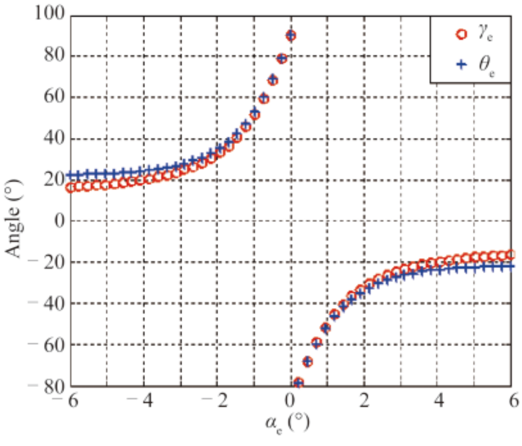

Fig. 5. Steady glide path angle, pitch angle vs. the steady angle of attack.

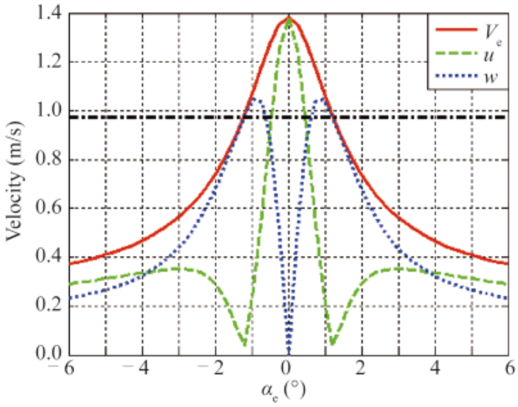

Fig. 6. Steady speed vs. the steady angle of attack.

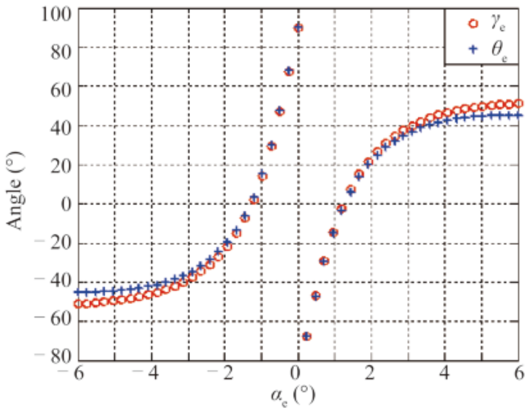

Fig. 7. Steady glide path angle, pitch angle vs. the steady angle of attack.

According to the comparative analysis interpreted in Fig. 4 and Fig. 6, in the hybrid-driven mode, the maximum steady speed increases obviously, whereas the corresponding range of the steady angle of attack reduces compared with the condition in the gliding mode. We can also derive the results from Fig. 5 and Fig. 7 that in the hybrid-driven mode, the ranges of the steady glide path angle and pitch angle increase, but the corresponding range of the steady angle of attack reduces compared with those produced in the gliding mode.

In addition, we can derive the relationship curves between the steady angle of attack of the Petrel-II HUG and the different propeller thrusts shown in Fig. 8. And as the propeller thrust increases, the steady angle of attack decreases. Furthermore, in Fig. 4, we can find that when the horizontal velocity reaches the maximum, the corresponding steady angle of attack is about –1.8°. Then as shown in Fig. 5, when the steady angle of attack is about –1.8°, the corresponding steady glide path angle is about 35°. The result is similar to the result shown in the literature (Graver, 2005). The above result is derived in the gliding mode.

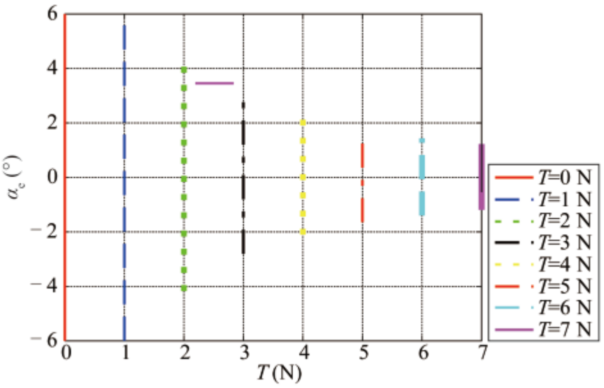

Fig. 8. Steady angle of attack vs. different propeller thrusts.

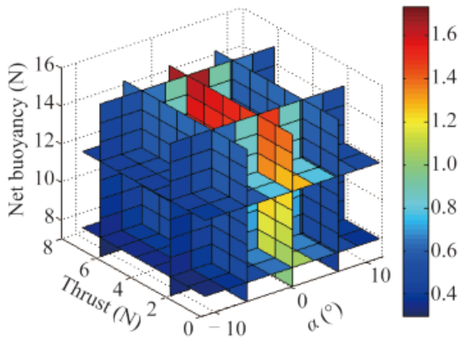

Fig. 9. Steady speed vs. the net buoyancy, propeller thrust and angle of attack.

When the HUG is working in the hybrid-driven mode and the horizontal velocity reaches the maximum, the corresponding steady angle of attack achieves –0.9° as shown in Fig. 6. Then as shown in Fig. 7, when the steady angle of attack arrives –0.9°, the corresponding steady glide path angle reaches 20°. In other words, when the horizontal velocity reaches the maximum, the corresponding steady glide path angle is smaller in the hybrid-driven mode than that in the gliding mode. Thus, if we want the HUGs to launch at the maximum horizontal velocity, we should set the target pitch angle at 20°.

According to Eq. (21), the steady speed with different net buoyancy, propeller thrust and angle of attack can be obtained as shown in Fig. 9.

As illustrated in Fig. 9, with the increase of the net buoyancy and propeller thrust, the maximum steady speed of the HUG increases, while on the contrary, the corresponding range of the steady angle of attack reduces. If we want to obtain larger velocity, we can also reduce the drag force of the HUG as far as possible. For example, a folding propeller can be selected (Chen et al., 2013, 2015).

According to the above hydrodynamic coefficients and the conditions that T=7 N, m_0=0.7 kg, K_{M0}=0.7959 kg and K_{M}=313.8643 kg/rad, submitting these parameters into Eqs. (21) and (22), it can be calculated that the steady speed V_{e}=1.3694 m/s, and that the steady glide path angle γ_{e}=1.339 rad. Furthermore, by calculating Inequalities (26)–(28), the results are obtained as: K'_{De}=3.6272 kg/m, V_{e}>0.9754 m/s, and $T_{\mathrm{e}}\leqslant$7.5732 N. The three inequalities are all satisfied. Namely, under the above conditions, the HUG can achieve the steady-state motion. Moreover, when $T_{\max}$=7.5732 N, V_{emax}=1.3968 m/s. Therefore, we can derive the result that when 0.9754 m/s<V<1.3968 m/s, the HUG can be stable.

In addition, under the conditions that K_q=–7 kg·s/rad, J_2=12.3 kg·m^2, m_1=84.7 kg, and m_3=84.7 kg, substituting these parameters into corresponding equations, the results of ε_1=1.308e^{-3} and ε_2=1.340e^{-3} can be derived, and then we can obtain $\mu=\max\{\varepsilon_1,\varepsilon_2\}=1.340\mathrm{e}^{-3}$.

If we consider a neighborhood of the equilibrium state, such as $\left|\overline{V}\right|\leqslant 0.2$, $|\bar{\alpha}|\leqslant 0.01$, $|\bar{q}|\leqslant 0.1$, and $\left|\bar{\gamma}\right|\leqslant \pi/4$, we can calculate μ_d=1.352e^{-3}, with d=0.9428. Since $\mu<\mu_d$, and referring to the above parameters, the Petrel-II HUG can be stable when working in the hybrid-driven mode.

Considering $|\overline{V}|\leqslant 0.2$, we can obtain that the range of V is 1.0955 m/s <V<1.6433 m/s. The result is compared with the range of V (0.9754 m/s <V<1.3968 m/s) derived by the inequalities. We can find that the range of the velocity derived by the method of the composite Lyapunov function is larger than that derived by the inequalities. Namely, the inequalities are relatively conservative at the lower bound of the velocity range.

Furthermore, under the condition that $\left|\bar{\gamma}\right|\leqslant\pi/4$ and $|\bar{q}|\leqslant 0.1$, whether the HUG is working in the hybrid-driven mode or gliding mode, we can estimate the maximum region of attraction. The results are shown in Figs. 10a and 10b.

As Fig. 10 indicates, the conclusions are drawn as follows.

When the range of $|\bar{\gamma}|$ and $|\bar{q}|$ remains unchanged, the maximum estimated region of $|\overline{V}|$ is larger in the gliding mode than that in the hybrid-driven mode. For the maximum estimated region of $|\bar{\alpha}|$, the situation is just opposite.

5 Field trials

We have carried out sea trials for 21 days with the Petrel-II HUG running in the gliding mode. It has obtained 219 consecutive profiles with a diving depth of 975 m and voyage of 626 km in the northern South China Sea from March 27 to April 16 in 2014. Fig. 11 shows the partial depth data measured by the CTD sensor equipped on the Petrel-II HUG, and the whole temperature data and depth data of the 219 consecutive profiles are described in Fig. 12. The results of the sea trials have shown that the Petrel-II HUG can work well in the gliding mode. Thus, the sea trials laid the foundation for the subsequent experiments with the HUG working in the hybrid-driven mode.

In the Danjiangkou Reservoir of China, we have carried

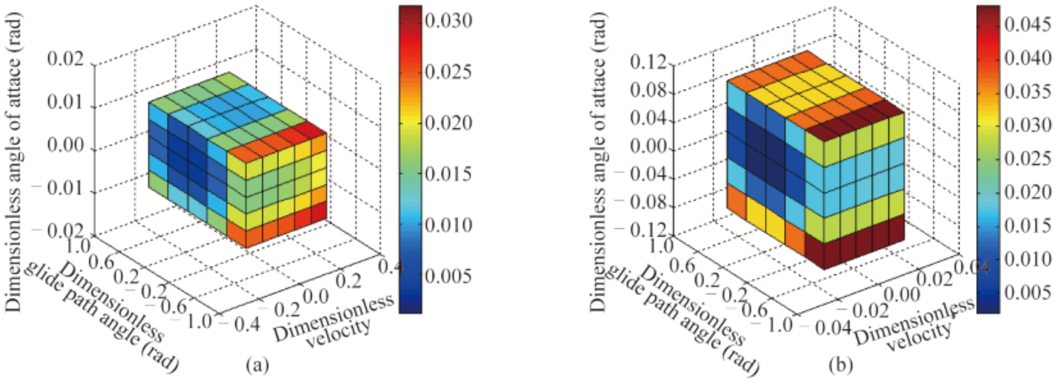

Fig. 10. (a) Region of attraction in the gliding mode, and (b) region of attraction in the hybrid-driven mode.

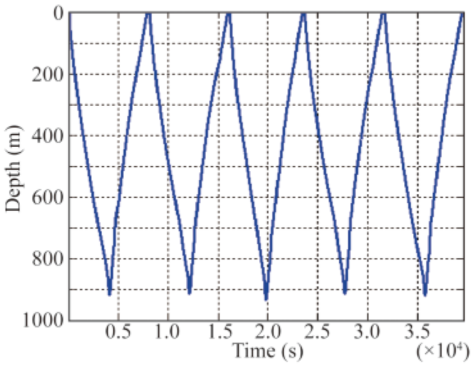

Fig. 11. Partial depth data measured by the CTD sensor.

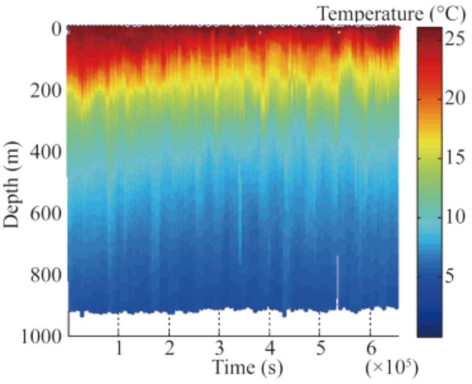

Fig. 12. Whole temperature and depth data of the 219 consecutive profiles.

out a dive test with a fixed depth from July 27 to July 31 in 2014. During the experiment, we set the target depth to 10 m, the net buoyancy to 2.5 N, and the target pitch angle to 0° in order to achieve the fixed depth sailing with the propeller speed of 780 rpm. The results are shown in Fig. 13. During the fixed depth voyage, the pitch angle changed between 2° and 5°. The steady pitch angle could reach about 3.5° on average. The actual depth changed between 0 m and 13.1 m. The average depth was about 11.3 m. And the steady speed was about 0.62 m/s on average. If the net buoyancy was set to 2.5 N, and the proper speed reached 800 rpm, according to the above corresponding equations, we could theoretically calculate the results: V_e=0.7979 m/s and the steady pitch angle θ_e=76.91°. And the range of the velocity derived by the inequalities was 0.5530 m/s<V<0.8347 m/s. The range of the velocity derived by the method of the composite Lyapunov function was 0.7939 m/s<V<0.8019 m/s and the range of the pitch angle was 0°≤θ_e≤90°. Since the theoretically calculated velocity and pitch angle were totally within the stable range, the Petrel-II HUG was stable via the above set parameters. But only the actual velocity was within the range derived by the inequalities. Thus, such fact further illustrates that the inequalities are relatively conservative at the lower bound of the velocity range. The theoretical values are larger than the actual values. One possible reason is that the effects of the internal battery pack have not been considered in this study. While by moving the battery pack, we could adjust the attitude of the HUG, then the actual angle of attack would be larger than the theoretical value, and the actual pitch angle and velocity would get smaller at the same time as shown in Fig. 6 and Fig. 7. Another possible reason may be that the Petrel-II HUG is equipped with water quality sensors below its abdomen. Thus the actual drag force would be larger than the theoretical value. Then the actual velocity would be smaller.

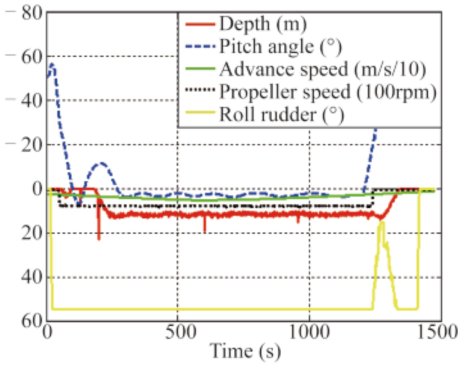

Fig. 13. Sailing results with the fixed depth.

We have also conducted sea trials of the Petrel-II HUG working in the hybrid-driven mode in the South China Sea from February 11 to February 16 in 2015. During the trials, we set the target depth to 500 m, the net buoyancy to 7 N, and the target pitch angle to ±45°. In the process of floating, we turned on the propeller and set the propeller speed to 1400 rpm. The results are shown in Fig. 14. When the propeller was working, the steady pitch angle could reach about +43.5° on average and the pitch angle had oscillation once, and the possible reason for this phenomenon is that the rotation of the internal battery pack causes the change of the pitch angle as shown in Fig. 14. And the steady speed was about 1.2 m/s on average. If the net buoyancy was 7 N, and the proper speed was 1400 rpm, according to the above corresponding equations, we could theoretically calculate the results: V_e=1.3743 m/s and θ_e=76.14°. And the range of the velocity derived by the inequalities conditions was 0.9825 m/s<V<1.3968 m/s. The range of the velocity derived by the method of the composite Lyapunov function was 1.0994 m/s<V<1.6492 m/s and the range of the pitch angle was 31.28°<θ_e<90°. Since the theoretically calculated and the actual velocity and pitch angle were totally within the stable range, the Petrel-II HUG was stable via the above setting parameters although the theoretical values were larger than the actual values. One possible reason is the same as the above analysis. Another possible reason may be that the yaw motion has been ignored while the HUG was adjusting the heading by rotating the internal battery pack. Then, the partial energy of the whole system was used for rolling, so that the energy used to improve the velocity and control the pitch angle was reduced as the whole energy was definite. In addition, there is a reason that the external environmental conditions are uncertain. All of these reasons can lead to larger theoretical values of the velocity and pitch angle.

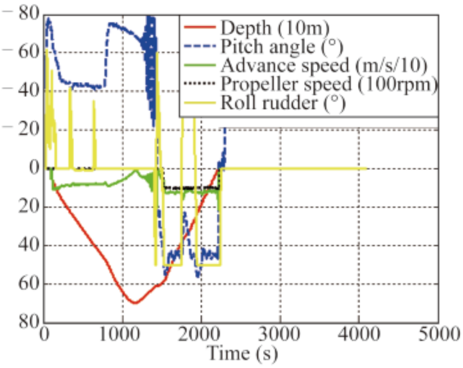

Fig. 14. Results of the hybrid-driven gliding.

6 Conclusions

In this paper, the Petrel-II HUG developed by Tianjin University is selected as the research object and the stability of the Petrel-II HUG in the hybrid-driven mode is theoretically proved based on the method of the composite Lyapunov function. Furthermore, we also calculate the steady-state operating conditions when the Petrel-II HUG reaches the desired steady-state motion.

The conclusions are drawn below:

(1) When the HUG working in the hybrid-driven mode, the maximum steady speed increases, while the corresponding range of the steady angle of attack decreases compared with the condition of working in the gliding mode.

(2) When the HUG working in the hybrid-driven mode, the ranges of steady glide path angle and pitch angle increase, while the corresponding range of the steady angle of attack decreases compared with the condition of working in the gliding mode.

(3) When the horizontal velocity reaches the maximum, the corresponding steady glide path angle is smaller in the hybrid-driven mode than that in the gliding mode.

(4) When the range of $\left|\bar{\gamma}\right|$ and $|\bar{q}|$ remains unchanged, the maximum estimated region of $\left|\bar{V}\right|$ is larger in the gliding mode than that in the hybrid-driven mode. For the maximum estimated region of $|\bar{\alpha}|$, the situation is just opposite.

(5) If we want to increase the velocity of the HUG, we should increase the net buoyancy and the propeller thrust.

The results of the sea trials show that the Petrel-II HUG has excellent performances no matter in the hybrid-driven mode or gliding mode. Then, we will further study the relationship between the stability and the design parameters of the HUG in order to improve the region of attraction. In a word, the HUG can be adopted for a wider range of marine environmental monitoring.

References

Alvarez, A., Caffaz, A., Caiti, A., Casalino, G., Gualdesi, L., Turetta, A. and Viviani, R., 2009. Folaga: A low-cost autonomous underwater vehicle combining glider and AUV capabilities, *Ocean Engineering*, 36(1), 24–38.

Bhatta, P. and Leonard, N.E., 2004. A Lyapunov function for vehicles with lift and drag: Stability of gliding, *Proceedings of the 43rd IEEE Conference on Decision and Control*, IEEE, Nassau, pp. 4101–4106.

Bhatta, P., 2006. *Nonlinear Stability and Control of Gliding Vehicles*, Ph. D. Thesis, Princeton University.

Bhatta, P. and Leonard, N.E., 2008. Nonlinear gliding stability and control for vehicles with hydrodynamic forcing, *Automatic*, 44(5), 1240–1250.

Caffaz, A., Caiti, A., Casalino, G. and Turetta, A., 2010. The hybrid glider/AUV Folaga, *IEEE Robotics & Automation Magazine*, 17(1), 31–44.

Caiti, A. and Calabro, V., 2010. Control-oriented modelling of a hybrid AUV, *Proceedings of 2010 IEEE International Conference on Robotics and Automation* (*ICRA*), IEEE, Anchorage, pp. 5275–5280.

Chen, Z.E., Yu, J.C., Zhang, A.Q., Yi, R. and Zhang, Q.F., 2013. Folding propeller design and analysis for a hybrid driven underwater glider, *Proceedings of 2013 OCEANS*, IEEE, San Diego, pp. 1–9.

Chen, Z.E., Yu, J.C., Zhang A.Q. and Song, S.M., 2015. Control system for long-range survey hybrid-driven underwater glider, *Proceedings of 2015 OCEANS*, IEEE, Genova, pp. 1–6.

Eriksen, C.C., Osse, T.J., Light, R.D. Wen, T., Lehman, T.W., Sabin, P.L., Ballard, J.W. and Chiodi, A.M., 2001. Seaglider: A long-range autonomous underwater vehicle for oceanographic research, *IEEE Journal of Oceanic Engineering*, 26(4), 424–436.

Fan, S.S., Wolek, A. and Woolsey, C.A., 2012. Stability and performance of underwater gliders, *Proceedings of 2012 OCEANS*, IEEE, Hampton, pp.1–10.

Graver, J.G., 2005. *Underwater Gliders*: *Dynamics*, *Control and Design*, Ph. D. Thesis, Princeton University, New Jersey, USA.

Isa, K. and Arshad, M. R., 2012. Neural networks control of hybrid-driven underwater glider, *Proceedings of 2012 OCEANS*, IEEE, Yeosu, pp. 1–7.

Isa, K. and Arshad, M.R., 2013. An analysis of homeostatic motion control system for a hybrid-driven underwater glider, *Proceedings of 2013 IEEE/ASME International Conference on Advanced Intelligent Mechatronics* (*AIM*), IEEE, Wollongong, pp. 1570–1575.

Isa, K., Arshad, M.R. and Ishak, S., 2014. A hybrid-driven underwater glider model. hydrodynamics estimation, and analysis of the motion control, *Ocean Engineering*, 81(2), 111–129.

Jenkins, S.A., Humphreys, D.E., Sherman, J., Osse, J., Jones, C., Leonard, N., Graver, J., Bachmayer, R., Clem, T., Carroll, P., Davis, P., Berry, J., Worley, P. and Wasyl, J., 2003. *Underwater Glider System Study*, Technical Report No. 53, Scripps Institution of Oceanography, University of California, San Diego, CA, 97–225.

Khalil, H.K., 1987. Stability analysis of nonlinear multiparameter singularly perturbed systems, *Proceedings of 1987 American Control Conference*, IEEE, Minneapolis, pp. 1219–1223.

Khalil, H.K. and Grizzle, J.W., 1996. *Nonlinear Systems*, Prentice hall, New Jersey, pp. 423–449.

Leonard, N.E. and Marsden, J.E., 1997. Stability and drift of underwater vehicle dynamics: Mechanical systems with rigid motion symmetry, *Physica D*: *Nonlinear Phenomena*, 105(1–3), 130–162.

Leonard, N.E., 1997a. Stability of a bottom-heavy underwater vehicle, *Automatica*, 33(3), 331–346.

Leonard, N.E., 1997b. Stabilization of underwater vehicle dynamics with symmetry-breaking potentials, *Systems & Control Letters*, 32(1), 35–42.

Leonard, N.E. and Graver J.G., 2001. Model-based feedback control of autonomous underwater gliders, *IEEE Journal of Oceanic Engineering*, 26(4), 633–645.

Liu, F., 2014. *System Design and Motion Behaviors Analysis of the Hybrid Underwater Glider*, Ph. D. Thesis, Tianjin University, Tianjin. (in Chinese)

Niu, W.D., Wang, Y.H., Yang, Y.P., Zhu, Y.Q. and Wang, S.X., 2016. Hydrodynamic parameter identification of hybrid-driven underwater glider, *Chinese Journal of Theoretical and Applied Mechanics*, 48(4), 813–822. (in Chinese)

Sherman, J., Davis, R.E., Owens, W.B. and Valdes, J., 2001. The autonomous underwater glider "Spray", *IEEE Journal of Oceanic Engineering*, 26(4), 437–446.

Wang, C.F., Zhang, F.M. and Schaefer, D., 2015. Dynamic modeling of an autonomous underwater vehicle, *Journal of Marine Science and Technology*, 20(2), 199–212.

Wang, T., 2012. *Research of Efficient Thruster of Deep Sea Unmanned Submersible*, Ph. D. Thesis, Harbin Engineering University, Harbin. (in Chinese)

Webb, D.C., Simonetti, P.J. and Jones, C.P., 2001. SLOCUM: An underwater glider propelled by environmental energy, *IEEE Journal of Oceanic Engineering*, 126(4), 447–452.

Woolsey, C.A. and Leonard, N.E., 2002. Stabilizing underwater vehicle motion using internal rotors, *Automatica*, 38(12), 2053–2062.

Zhao, B., Wang, X., Yao, B. and Lian, L., 2015. Lyapunov stability analysis of the underwater glider, *Journal of Harbin Engineering University*, 36(1), 83–87. (in Chinese)

Appendix A. Interconnection conditions

We denote the left-hand side of Condition (i) by $C_{\mathrm{in},\,1}$. We calculate

$$\begin{aligned}
C_{\mathrm{in},1} &= \frac{\partial V}{\partial x}[f(t,x,y,\varepsilon)-f(t,x,h(t,x),0)] = \frac{\partial V}{\partial x}[f(x,y)-f(x,0)] \\
&= \frac{\{K_{\mathrm{D}}[-(\bar{\alpha}+\alpha_{\mathrm{e}})^2+\alpha_{\mathrm{e}}^2]+u_{2\mathrm{e}}[-\cos\alpha_{\mathrm{e}}+\cos(\bar{\alpha}+\alpha_{\mathrm{e}})]\}(1+2\overline{V}+\overline{V}^2-\cos\overline{\gamma})}{K'_{\mathrm{De}}}(1+\overline{V})^2 \\
&\quad + \frac{\{-K_{\mathrm{L}}\bar{\alpha}+u_{2\mathrm{e}}[-\sin\alpha_{\mathrm{e}}+\sin(\bar{\alpha}+\alpha_{\mathrm{e}})]\}\sin\overline{\gamma}}{K'_{\mathrm{De}}}(1+\overline{V})^2 \\
&\leqslant \left[\frac{K_{\mathrm{D}}}{K'_{\mathrm{De}}}(|\overline{\alpha}_{\max}|+2|\alpha_{\mathrm{e}}|)+\frac{u_{2\mathrm{e}}}{K'_{\mathrm{De}}}H\right]\left[\left(\sqrt{2}+1\right)\overline{V}_{\max}+\sqrt{2}\right]\varphi(\cdot)\phi(\cdot) \\
&\quad + \left(\frac{K_{\mathrm{L}}}{K'_{\mathrm{De}}}+\frac{u_{2\mathrm{e}}}{K'_{\mathrm{De}}}H'\right)\varphi(\cdot)\phi(\cdot) = \beta_1\varphi(\cdot)\phi(\cdot), \qquad \text{(A1)}
\end{aligned}$$

where, $\beta_1 = \dfrac{K_{\mathrm{D}}(|\bar{\alpha}_{\max}|+2|\alpha_{\mathrm{e}}|)+u_{2\mathrm{e}}H}{K'_{\mathrm{De}}}\left[(\sqrt{2}+1)\bar{V}_{\max}+\sqrt{2}\right]+\dfrac{K_{\mathrm{L}}+u_{2\mathrm{e}}H'}{K'_{\mathrm{De}}}$, $\phi(\cdot)=(1+\overline{V})\sqrt{\bar{\alpha}^2+\bar{q}^2}$,

$\varphi(\cdot)=\sqrt{(\overline{V}+2)^2\overline{V}^2+4(1+\overline{V})^2\sin^2\left(\frac{\bar{\gamma}}{2}\right)}$, $H=\sin^2\dfrac{\alpha_{\max}}{2}+\sin^2\left(\dfrac{\alpha_{\max}}{2}+|\alpha_{\mathrm{e}}|\right)$, $\gamma_1=0$, and $H'=\sin^2\left(\dfrac{\alpha_{\max}}{2}\right)+\cos^2\left(\dfrac{\alpha_{\max}}{2}+|\alpha_{\mathrm{e}}|\right)$.
Using the above results in Eq. (A1), we find that Condition (i) holds.

We denote the left-hand side of Condition (ii) by $C_{\mathrm{in},\,2}$. We calculate

$$\begin{aligned}C_{\mathrm{in},2} &= \frac{\partial \hat{W}}{\partial z}A[g(x,y,\varepsilon)-g(x,y,0)]\\
&= \frac{\mu(c_1\bar{\alpha}+c_3\bar{q})}{K'_{\mathrm{De}}V_{\mathrm{e}}^2(1+\overline{V})}\left\{-m_0 g\cos(\bar{\gamma}+\gamma_{\mathrm{e}})+[K_{\mathrm{L0}}+K_{\mathrm{L}}(\bar{\alpha}+\alpha_{\mathrm{e}})-u_{2\mathrm{e}}\sin(\bar{\alpha}+\alpha_{\mathrm{e}})]V_{\mathrm{e}}^2(1+\overline{V})^2\right\}\\
&\leqslant \frac{\mu(c_1+c_3)}{K'_{\mathrm{De}}(1+\overline{V})^3}\left\{|K_{\mathrm{Le}}|\left[(\sqrt{2}+1)\overline{V}_{\max}+\sqrt{2}\right]+|u_{2\mathrm{e}}|\left[\left(\sqrt{2}+1\right)(\overline{V}_{\max}+1)+1\right]+|K_{\mathrm{De}}|\right\}\varphi(\cdot)\phi(\cdot)\\
&+\frac{\mu K_{\mathrm{L}}(2c_1+c_3)}{2K'_{\mathrm{De}}(1+\overline{V})}\phi^2(\cdot)\leqslant \mu\gamma'_2\phi^2(\cdot)+\mu\beta'_2\varphi(\cdot)\phi(\cdot),\end{aligned} \tag{A2}$$

where $\beta'_2=\frac{(c_1+c_3)}{K'_{\mathrm{De}}(1+\overline{V}_{\min})^3}\left\{|K_{\mathrm{Le}}|\left[\left(\sqrt{2}+1\right)\overline{V}_{\max}+\sqrt{2}\right]+|u_{2\mathrm{e}}|\left[\left(\sqrt{2}+1\right)(\overline{V}_{\max}+1)+1\right]+|K_{\mathrm{De}}|\right\}$, $\gamma'_2=\frac{K_{\mathrm{L}}(2c_1+c_3)}{2K'_{\mathrm{De}}(1+\overline{V}_{\min})}$, and $c_1=1+2r_2(1+\overline{V})^2/r_1, c_2=1+r_1/(r_2 a)$, and c_3=1. With the above results of Eq. (A2), Condition (ii) is satisfied.

We denote the left-hand side of Condition (iii) by $C_{\mathrm{in},\,3}$. We calculate

$$\begin{aligned}C_{\mathrm{in},3}&=\left|\left[\frac{2\bar{\alpha}^2 r_2}{r_1}(1+\overline{V})-\frac{r_1\bar{q}^2}{r_2}\frac{1}{(1+\overline{V})^3}\right]\left\{\frac{K'_{\mathrm{De}}\sin\bar{\gamma}+K'_{\mathrm{De}}[\cos\bar{\gamma}-(1+\overline{V})^2]}{K'_{\mathrm{De}}}\right\}\right|\\
&\leqslant\left|\frac{2H'' r_2}{r_1}\frac{1}{(1+\overline{V})}\right|\phi^2(\cdot)+\left|\frac{r_1 H''}{r_2(1+\overline{V})^5}\right|\phi^2(\cdot)\leqslant\gamma''_2\phi^2(\cdot),\end{aligned} \tag{A3}$$

with $\gamma''_2=\max\left[\left|\frac{2H''r_2}{r_1(1+\overline{V})}\right|+\left|\frac{r_1H''}{r_2(1+\overline{V})^5}\right|\right]=\left|\frac{2H''{}_{\max}r_2}{r_1(1+\overline{V}_{\min})}\right|+\left|\frac{r_1H''{}_{\max}}{r_2(1+\overline{V}_{\min})^5}\right|$, and $\beta''_2=0$,

where $H''_{\max}=\left|\frac{\left|\max(K'_{\mathrm{Le}}\sin\bar{\gamma})\right|+K'_{\mathrm{De}}\max[\cos\bar{\gamma}-(1+\overline{V})^2]}{K'_{\mathrm{De}}}\right|$. Then according to the above results of Eq. (A3), Condition (iii) holds.